SUPPLEMENTARY DATA

SUPPLEMENTARY METHODS

Single Particle Analysis of HASt-LTV1 pre-40S particles : 2D and 3D Classification assays.

In a first approach, the 103,247 particles dataset was submitted to various 3D classifications experiments (Supplementary Figure S1). In order to determine the number of structural conformers, 3D classifications were performed using a 60 Å low-pass filtered human 40S subunit (PDB code: 4V6X (1)), devoid of RPS26 and RPS10, as initial model. The number of generated 3D classes varied from 4 to 15. Indeed, increasing the number of 3D classes should yield redundant structures when reaching and exceeding the actual number of conformers in solution (77). However, redundant classes were never clearly distinguished, as neither were radically different nor strictly similar, as exemplified for a number of classes K=4 in Supplementary Figure S1A .

Each 3D classification was replicated. In RELION 1.3, the 3D classification is realized through an initial random distribution of the particles within the given number of 3D classes. Thus, if the population of particles is composed by a finite number of conformers, the final products of several classifications should yield the same 3D classes, regardless of the initial randomisation step (77). Supplementary Figure S1A represents a duplicate 3D classification. The number of iterations was optimized to 30 and the angular step search to 7,5°, to yield stable classes while avoiding data overfitting. Final resolution (according to the SSNR > 1 criterion) was 27 Å for Replicate A (upper panel) and 26 Å for replicate B (lower panel). While the classes appear globally similar between both replicates, local variations are clearly distinguishable, on both the solvent and the interface views of the structures. These variations, indicated by arrowheads, are mostly localized where the pre-ribosomal factors have been attributed, and are coherent with the local resolution drop-down (See Figures 2C and S2B), suggesting hypervariability of these regions. Moreover, further refinement of these 3D classes never yielded better resolution than 20 Å, even after many trials of grouping and/or sub-classify them (Supplementary Figure S1A, bottom raw). Inspection of the orientations repartition of the particles within each 3D class suggest that 3 out of the 4 3D classes lack views from the solvent (classes K1, K2 and K4 in Supplementary Figure S1B), as well as from the 60S interface. These missing orientations are reinforced within the self-refined models (not shown), and might partly prevent reaching a higher resolution.

In a second approach, two successive reference-free 2D classifications were performed to get rid of defective particles, resulting in a dataset of 58,436 particles (Supplementary Figure S1C). A refinement procedure was directly applied to this dataset, using the same initial model as before. This resulted in a consensus 3D structure of 22.9 Å resolution at FSC = 0.143, according to the gold standard FSC procedure

(30,31). This 3D structure was then masked with an *ad hoc* binarized soft mask (with a 10 pixels fall-off), by using the post-process command of RELION 1.3, which gave rise to a 19.4 Å resolution structure at FSC = 0.143 (Supplementary Figure S2). In order to distinguish structural variants within the particles yielding this consensus structure, several 3D classifications assays were then performed with a number of classes ranging from 4 to 8, and each classification was repeated twice. This time, only a minority of the resulting 3D classes were overlapping between both replicates (Supplementary Figure S1D, classes K5 and K7). Refinement of the majority class (K5) led to a 21 Å resolution 3D structure, which could not be further sorted out by 3D classification (not shown).

SUPPLEMENTARY REFERENCES

77. Scheres,S.H.W. (2010) Classification of structural heterogeneity by maximum-likelihood methods. *Meth. Enzymol.*, **482**, 295–320.

SUPPLEMENTARY FIGURE LEGENDS

Supplementary Figure S1. 3D Classification replicates suggest a strong continuous heterogeneity within the HASt-LTV1 pre-40S cryo-EM images dataset.

(A), 3D classification duplicates of the whole dataset into 4 structural variants (K1-K4). The 3D classes are displayed along the solvent side view. Classes of replicate B (lower panel) have been re-ordered according to conformational similarities with the classes generated in replicate A (upper panel). Arrowheads indicate local variations between both replicates. **(B),** Angular distribution of the particles included in each 3D class of replicate B. Each cylinder represents an Euler angle, colored according to the number of particles oriented along this angle (blue: few particles, red: many particles). Missing points among the pattern of cylinders mean that no particles have been attributed to these orientations. **(C),** Image processing scheme performed to obtain the 19 Å resolution 3D consensus structure analyzed in this article. Orientations of the particles encompassed within the 3D structure are shown in the right panels. **(D),** Duplicate of 3D Classification of the 58,436 particles dataset presented in **(C)**. The consensus 3D structure obtained in **(C)** was low-pass filtered to 40 Å resolution and used as an initial reference for each replicate of 3D classification. The bottom row indicates the resolution obtained after refinement of classes K5 and K7 of replicate B.

Supplementary Figure S2. Resolution of HASt-LTV1 pre-40S cryo-EM 3D structure, and comparison to other known 3D models.

(A), Gold-standard Fourier Shell Correlation (FSC) curve for the HASt-LTV1 pre-40S complex, after 3D refinement and postprocessing in RELION (29). **(B),** Cutaway view from the 60S interface of the unfiltered HASt-LTV1 pre-40S final map, colored according to local resolution calculated with the ResMap software package (32). **(C)**, Difference map (grey densities) between the HASt-LTV1 pre-40S 3D structure and the human mature 40S 3D structure (PDB code: 4V6X) filtered at 21 Å resolution (pale blue density). Only positive differences, corresponding to extra-densities of the pre-40S map have been displayed, with a threshold of 1σ. **(D)**, Superimposition of the human HASt-LTV1 pre-40S 3D structure (grey) and its yeast counterpart (purple), purified by using Rio2-TAP as bait and solved at 18 Å resolution (EMDB code: 1927). This superimposition was performed by using the "Fit" command of Chimera. Additional density on the beak region of the human pre-40S particle is indicated by a grey arrow on the solvent view. On the interface view, domains attributed to RIO2/Rio2 on the human and the yeast pre-40S particles are indicated by white and dark purple arrows, respectively.

Supplementary Figure S3. Analysis of ribosome biogenesis factors associated to HASt-LTV1 pre-40S particles.

(A), General view from the beak of the HASt-LTV1 pre-40S 3D model (left panel) and close-up on the region framed by a black rectangle (right panel). The X-Ray structure of SelB from *M. maripaludis* (PDB code: 4AC9) fitted by rigid body docking into the density zone attributed to TSR1 is displayed in pink. Docking of the X-Ray structure of Rio2 from *C. thermophilum* (PDB code: 4GYI, lime green), obtained by the same method. The position of Rio2 presented here is the best solution, according to the correlation coefficient given by the command "Fit" of Chimera. **(B),** The predicted 3D structure of human NOB1 (yellow) has been aligned to the NMR structure of *P. horikoshii* Nob1, (PDB code: 2LCQ, blue), with the "MatchMaker" option from Chimera. The PIN domain intrinsic loop and the C-terminal unstructured stretch of human NOB1, absent from the archaeal atomic model, have been shortened on the figure and symbolized by dotted lines. **(C)**, Surface view of the 3D consensus structure of HASt-LTV1 pre-40S particles, calculated by using an initial model devoid of RACK1, RPS10 and RPS26. **(D),** As a comparison, the 3D structure of this "RACK1-less" mature 40S subunit has been scaled to the same pixel size, low-pass filtered at 21-Å resolution, and displayed along identical orientations. **(C-D)**, Position of RACK1 on the head of the mature 40S subunit is indicated by black ellipses.

Supplementary Figure S4. Relative efficiency of different siRNAs targeting RACK1 mRNA.

RT-qPCR was conducted on total RNA extracts obtained 48 h or 72 h after treatment with 3 different siRNAs

targeting RACK1, an siRNA targeting RPS15 mRNA, or a scramble siRNA without target. The following primer set was used: 5'-GGGACAAGCTGGTCAAGGTA-3' (forward); 5'-GGGATCCATCTGGAGAGACA-3' (reverse). The results are expressed as the proportion of remaining RACK1 mRNAs relative to control. For each depletion condition, the impact on the protein level was assessed by Western blot, relative to actin.

Supplementary Figure S1

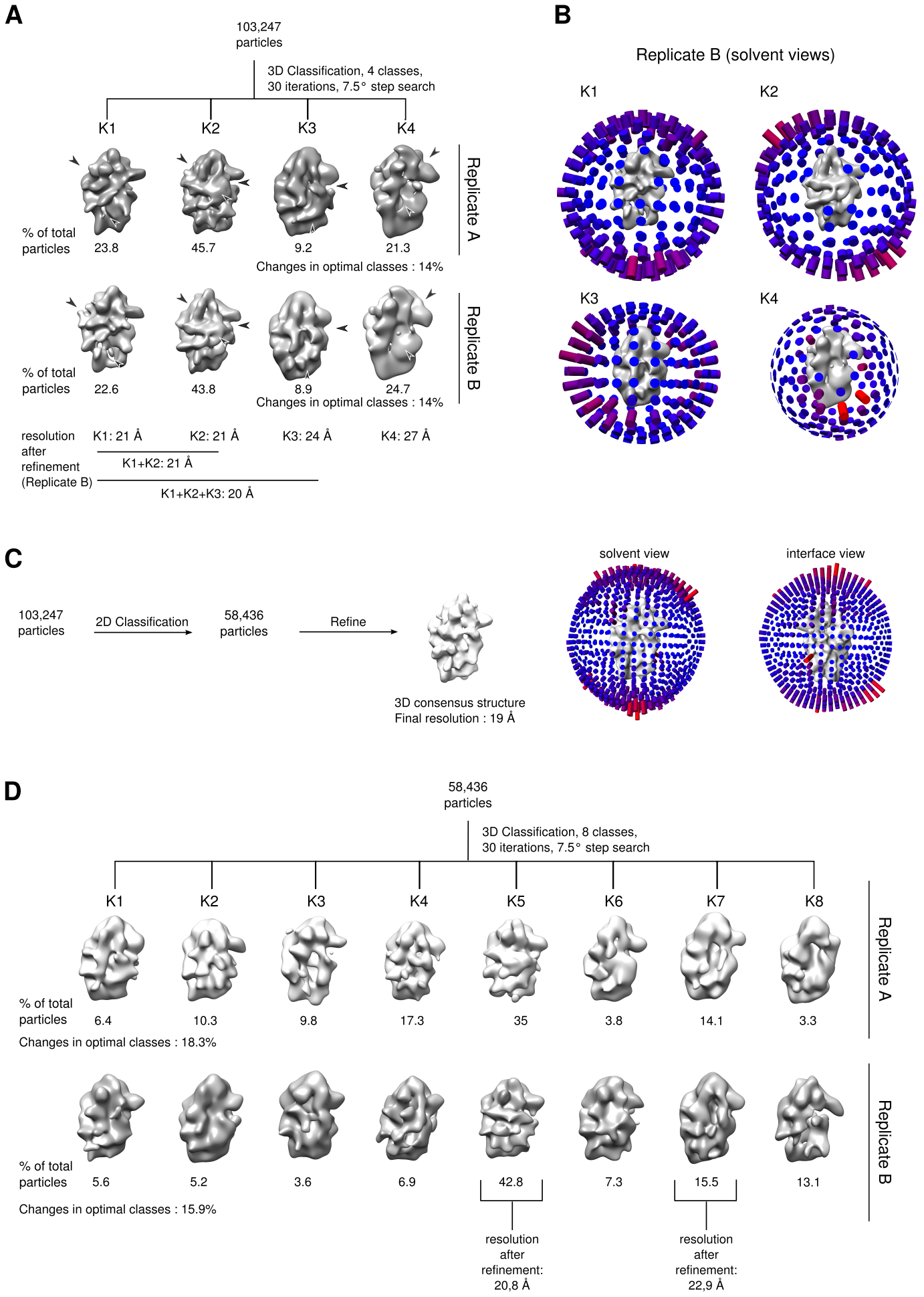

Supplementary Figure S2

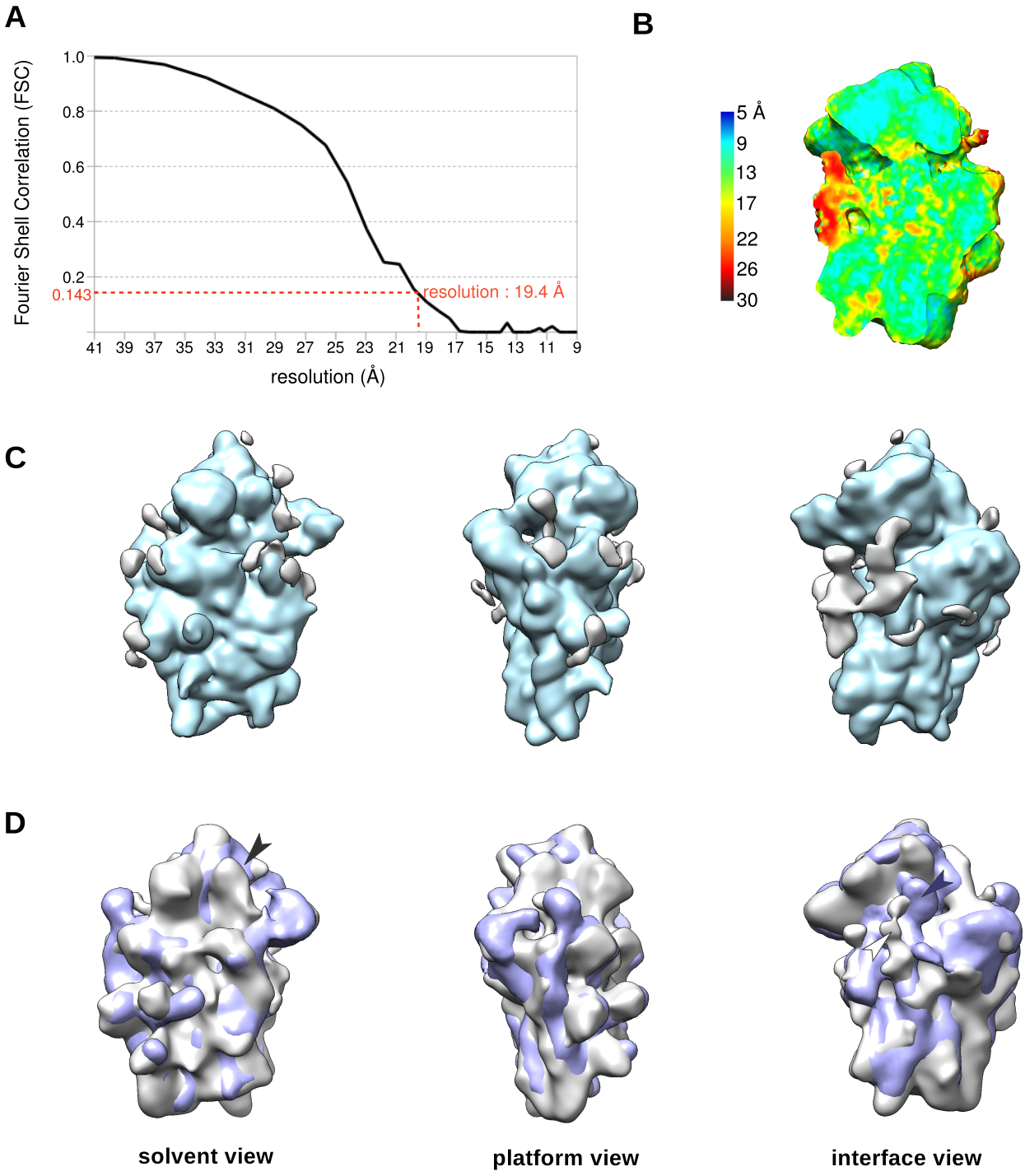

Supplementary Figure S3

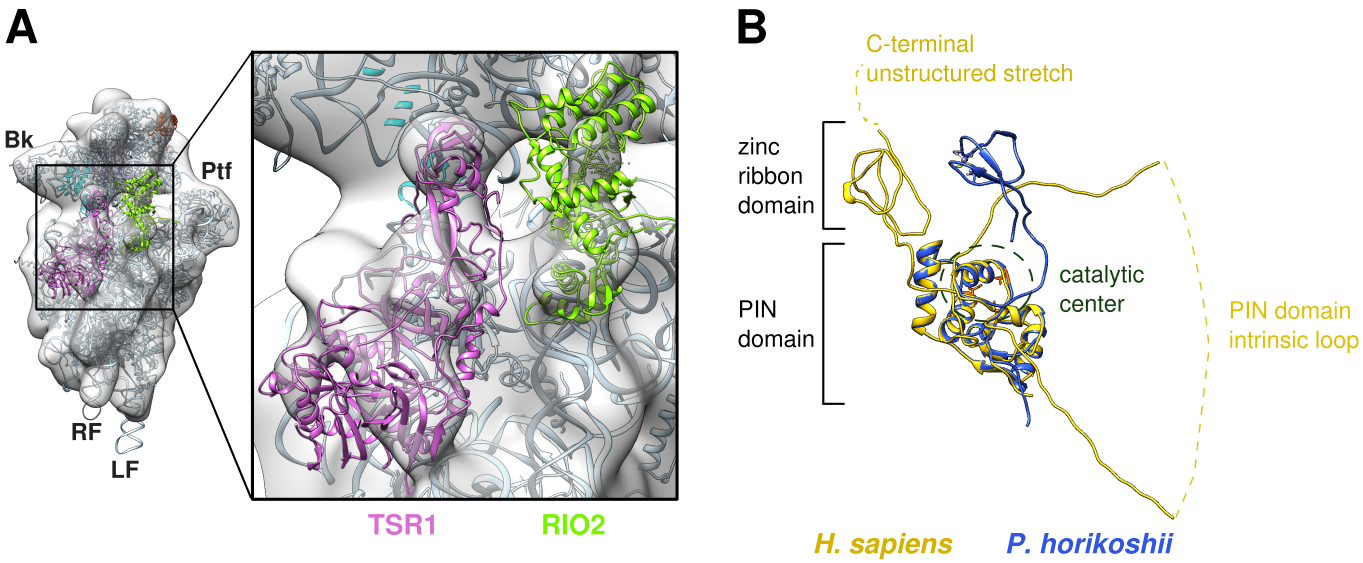

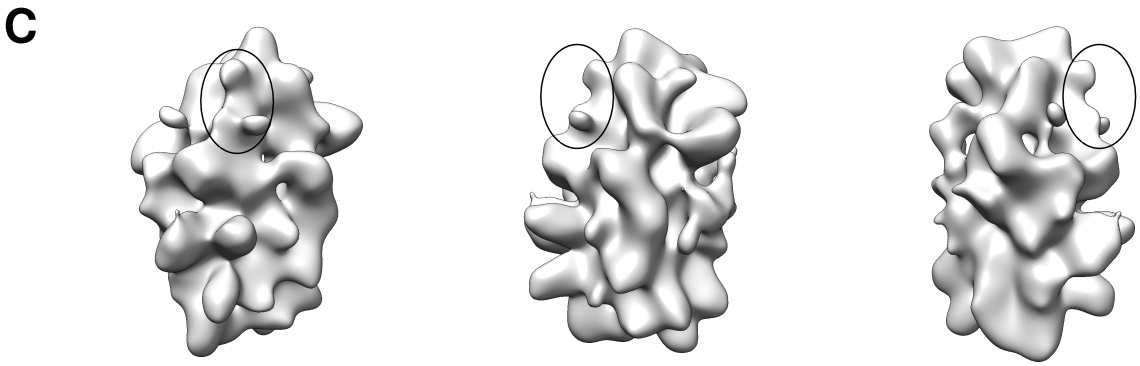

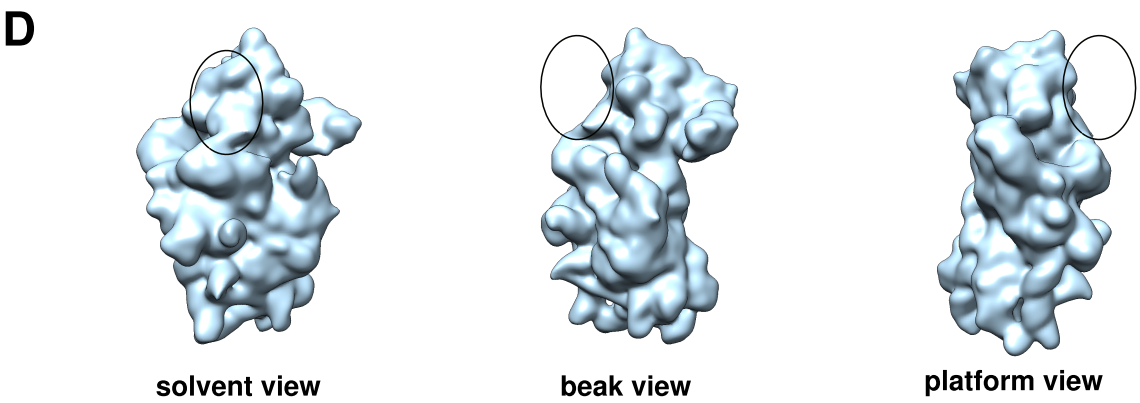

Supplementary Figure S4